



Structural transformation of a lithium-rich $\text{Li}_{1.2}\text{Co}_{0.1}\text{Mn}_{0.55}\text{Ni}_{0.15}\text{O}_2$ cathode during high voltage cycling resolved by *in situ* X-ray diffraction

Debasish Mohanty^{a,*}, Sergiy Kalnaus^{a,**}, Roberta A. Meisner^a, Kevin J. Rhodes^b, Jianlin Li^a, E. Andrew Payzant^c, David L. Wood III^a, Claus Daniel^{a,d,e}

^a Materials Science and Technology Division, Oak Ridge National Laboratory, Oak Ridge, TN 37831-6083, USA

^b Ford Research and Innovation Center, Ford Motor Company, Dearborn, MI 48121, USA

^c Chemical and Engineering Materials Division, Oak Ridge National Laboratory, Oak Ridge, TN 37831-6475, USA

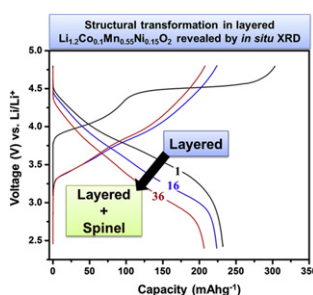
^d Energy and Transportation Science Division, Oak Ridge National Laboratory, Oak Ridge, TN 37831-6083, USA

^e Bredeben Center for Interdisciplinary Research and Graduate Education, University of Tennessee, Knoxville, TN 37996, USA

HIGHLIGHTS

- ▶ Structural transformation in lithium rich NMC cathode was investigated by *in situ* XRD.
- ▶ The constant *a*-lattice parameter was observed during first cycle charging (4.4 V–4.7 V).
- ▶ Decrease in *c*-lattice parameter value was observed beyond 4.4 V charging.
- ▶ Spinel peaks were detected during low voltage discharge process after subsequent cycles.
- ▶ Layered to spinel phase transformation suppresses the voltage profile in subsequent cycles.

GRAPHICAL ABSTRACT



ARTICLE INFO

Article history:

Received 25 September 2012

Received in revised form

19 November 2012

Accepted 28 November 2012

Available online 12 December 2012

Keywords:

In situ XRD

Li-rich NMC

High-voltage cycling

Phase transformation

Spinel

ABSTRACT

Lithium-rich layered oxides having compositions of $\text{Li}_{1+y}\text{M}_{1-y}\text{O}_2$ ($\text{M} = \text{Co}, \text{Mn}, \text{and Ni}$) have become attractive cathode materials for high energy density and high voltage lithium ion batteries for electric vehicle (EV) applications. However, their utility in EVs suffers from both voltage and capacity fade. The voltage fade is related to structural transformation in these lithium-rich oxides and must be thoroughly understood. In this work, we have utilized *in situ* X-ray diffraction in order to monitor these structural transformations during high voltage (4.8 V) cycling of a lithium- and manganese-rich $\text{Li}_{1.2}\text{Co}_{0.1}\text{Mn}_{0.55}\text{Ni}_{0.15}\text{O}_2$ oxide cathode, which has not been reported previously. The lattice parameters of the cathode were monitored for first cycle and compared with the subsequent cycles. Based on our results, the *c*-lattice parameter increases during the course of initial charging and eventually decreases upon charging beyond 4.4 V, which verifies lithium extraction occurs from transition metal layers due to activation of Li_2MnO_3 phase at high-voltage. The fact that the *a*-lattice parameter remains constant at the first cycle plateau region indicates oxygen loss from the structure during first cycle charging which is attributed to irreversible capacity obtained from first cycle. For first and subsequent cycles, the *c*-lattice parameter

* Corresponding author. Tel.: +1 865 576 0813.

** Corresponding author. Tel.: +1 865 576 6181.

E-mail addresses: mohanty@ornl.gov (D. Mohanty), Kalnaus@ornl.gov (S. Kalnaus).

increases during discharge up to 3.5 V and below 3.5 V, the decrease in those values was observed. After subsequent cycling, (440) cubic spinel reflections were observed during low voltage discharge process, which reveals a layer to spinel-like phase transformation in the lattice and is thought to be the reason for the observed voltage fade. A significant decrease in monoclinic phase was observed after subsequent cycles and is believed to contribute to the structural instability and capacity fade after repeated cycling.

Published by Elsevier B.V.

1. Introduction

For the past several years, rechargeable lithium ion battery (LIB) technology has been the most widely used energy storage method for powering consumer electronics and power tools [1,2]. Two dimensional layered oxide materials having the chemical formula LiMO_2 ($M = \text{Co}, \text{Mn}, \text{Ni}$) have been extensively utilized and studied as cathode materials for LIBs for several decades [3–6]. However, because of their limited capacity, limited energy density, and safety concerns, these cathode materials fail to meet the necessary demands for LIBs to power electric vehicles (EVs) [6–8]. To realize the energy needs for on-board energy storage technology in EVs, “lithium-rich” oxide cathode materials have been developed [9–12]. These lithium-rich oxide compounds are generally represented as $\text{Li}_{1+y}\text{M}_{1-y}\text{O}_2$ ($M = \text{Co}, \text{Mn}, \text{Ni}$), which are two-component composites between $z\text{Li}_2\text{MnO}_3$ and $(1-z)\text{LiMO}_2$ ($M = \text{Co}, \text{Mn}, \text{Ni}$) as proposed by Thackeray and co-workers [11,13]. As an example, the lithium- and manganese-rich oxide in this work is $\text{Li}_{1.2}\text{Co}_{0.1}\text{Mn}_{0.55}\text{Ni}_{0.15}\text{O}_2$, or $0.5\text{Li}_2\text{MnO}_3-0.5\text{LiNi}_{0.375}\text{Co}_{0.25}\text{Mn}_{0.375}\text{O}_2$ in the two-component system notation (hereafter abbreviated as “lithium-rich NMC”). Lithium-rich oxides are among the most appealing cathode materials, and can deliver higher capacity ($>230 \text{ mA h g}^{-1}$) with an operating voltage higher than 3.5 V vs. Li/Li^+ as compared to the two-dimensional layered stoichiometric (non-composite) LiMO_2 cathodes [14,15]. It has also been observed that the Li_2MnO_3 phase becomes electrochemically active at higher voltage ($\geq 4.6 \text{ V}$) and can contribute towards the irreversible capacity loss in the first cycle [16,17].

Li_2MnO_3 and LiMO_2 both crystallize in layered rocksalt structures but differ in the space group symmetry depending on the ordering of ions in the unit cell [11]. Li_2MnO_3 (can also be written as $\text{Li}[\text{Li}_{1/3}\text{Mn}_{2/3}]\text{O}_2$) belongs to a monoclinic crystal system with $C2/m$ space group symmetry and LiMO_2 belongs to a trigonal (rhombohedral) crystal system with $R\bar{3}m$ space group symmetry [18]. In the case of Li_2MnO_3 , the Li^+ and Mn^{4+} ions occupy the transition metal layer, whereas for the LiMO_2 structure, the transition metal layers are occupied by only transition metal ions (as shown in Fig. 1). However, these two structures have similar cubic closed-packed layers with interlayer spacing of $\sim 4.7 \text{ \AA}$ ((001) for monoclinic and (003) for trigonal), which allows for integration of these structures at an atomic level to form $\text{Li}_{1+y}\text{M}_{1-y}\text{O}_2$ ($M = \text{Co}, \text{Mn}, \text{Ni}$)

[11]. In general, the structure of lithium-rich $\text{Li}_{1+y}\text{M}_{1-y}\text{O}_2$ ($M = \text{Co}, \text{Mn}, \text{Ni}$) can be derived from layered LiMO_2 (for example $M = \text{Co}$) with the $\alpha\text{-NaFeO}_2$ structure, with the excess lithium ions present in the structure occupying the transition metal layer, filling all the octahedral sites of the cubic close-packed oxygen arrays. The presence of lithium ions in the transition metal layer generates long-range/short-range cation ordering between transition metal ions forming the Li_2MnO_3 phase [19]. Despite the success of these lithium-rich oxide cathode materials in delivering high initial capacity, both capacity and voltage fade have been observed during subsequent electrochemical cycles [15,20,21]. Structural transformations in cathode materials play a vital role in the long-term performance of electrochemical storage systems based on such materials. Extensive research has been carried out addressing the structural transformation in lithium-rich materials during electrochemical cycling [15,19,21,22]. By combining computational and experimental methods, Xu et al. reported the formation of a spinel-like phase on the surface of $\text{Li}[\text{Ni}_x\text{Li}_{1/3-2x/3}\text{Mn}_{2/3-x/3}]\text{O}_2$ ($0 < x < 1/2$) particles after high-voltage cycling and proposed that this was the cause of the poor rate capacity [19]. In another study, Yabuchi et al. reported electrochemical reduction of oxygen at the electrode surface and ultimately formation of lithium carbonate during the discharge process below 3 V, which would need to be controlled in order to improve the cyclability of these cathode materials [15]. There are still open questions that must be addressed in order to understand the performance of the lithium-rich cathodes. The reasons for voltage fading and first-cycle irreversible capacity in these lithium-rich cathodes remain elusive and need to be elucidated, which is the motivation behind this work. It should be emphasized that the majority of studies on lithium-rich cathodes were based on *ex situ* techniques, thus obscuring the real time structural transformations leading to the final state. In this work, we have utilized *in situ* techniques to monitor the structural transformation in $\text{Li}_{1.2}\text{Co}_{0.1}\text{Mn}_{0.55}\text{Ni}_{0.15}\text{O}_2$ lithium-rich system during electrochemical cycling.

In situ X-ray diffraction (XRD) is a proven technique for the study of structural changes in oxide cathode materials [8,23–25]. The uniqueness of *in situ* XRD when applied to LIBs lies in the ability to monitor in real-time the structural transformations, changes in lattice parameters, and phase composition during electrochemical charge/discharge experiments, and it has been proven to be a versatile

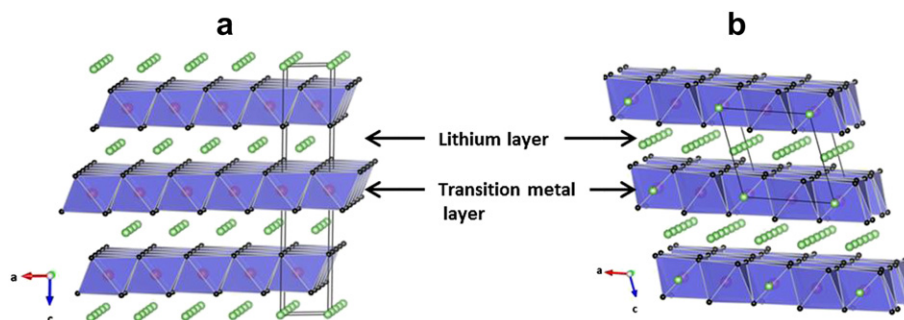


Fig. 1. Crystal structure of (a) layered trigonal LiMO_2 and (b) layered monoclinic Li_2MnO_3 . In Li_2MnO_3 structure, lithium ions occupy transition metal layer as well as lithium layer.

technique for the study of oxide cathode materials [26]. Previously, Dahn's group has studied the change in the lattice parameter with *in situ* XRD during the electrochemical cycling of $\text{Li}[\text{Ni}_x\text{Li}_{(1/3-2x/3)}\text{Mn}_{(2/3-x/3)}]\text{O}_2$ [23]. Recently, by utilizing similar methods, Fell et al. reported the dynamic strain change due to migration of lithium and transition metal ions in $\text{Li}[\text{Li}_{0.2}\text{Ni}_{0.2}\text{Mn}_{0.6}]\text{O}_2$ material during the first cycle [24]. In research from our group, a novel *in situ* XRD cell was designed and first tested with a silicon anode material [27], as well as spinel $\text{Li}(\text{Mn}_{1.5}\text{Ni}_{0.5})\text{O}_4$ cathode material in order to observe the phase transformations during electrochemical cycling [28]. However, these previous studies were limited to binary lithium-rich materials. To our knowledge, detailed *in situ* XRD of ternary lithium-rich cathodes such as $\text{Li}_{1.2}\text{Co}_{0.1}\text{Mn}_{0.55}\text{Ni}_{0.15}\text{O}_2$ ($0.5\text{Li}_2\text{MnO}_3-0.5\text{LiNi}_{0.375}\text{Co}_{0.25}\text{Mn}_{0.375}\text{O}_2$) investigated in this work has not yet been reported. *In situ* XRD studies were performed on a fresh electrode and during subsequent cycles in order to: 1) monitor the change in lattice parameters upon electrochemical lithiation/delithiation; 2) explain the reason for the first cycle irreversible capacity loss; and 3) determine mechanisms of structural change that result in voltage fade with increased cycle number. This study provides valuable information about real-time structural transformation during electrochemical cycling of a $\text{Li}_{1.2}\text{Co}_{0.1}\text{Mn}_{0.55}\text{Ni}_{0.15}\text{O}_2$ cathode, and will be instrumental in development and/or modification of the parent structure of the lithium-rich cathode oxides in the series of $z\text{Li}_2\text{MnO}_3-(1-z)\text{LiMO}_2$ ($\text{M} = \text{Co}, \text{Mn}, \text{Ni}$) for better electrochemical performance.

2. Experimental

2.1. *In situ* electrochemical X-ray diffraction

The electrodes used for *in situ* studies were fabricated at Argonne National Laboratory using lithium-rich NMC powder ($\text{Li}_{1.2}\text{Co}_{0.1}\text{Mn}_{0.55}\text{Ni}_{0.15}\text{O}_2$) made by TODA America Inc (designated as "Toda HE5050"). The electrode composition was as follows: 86 wt% HE5050, 8 wt% Solvay 5130 PVDF binder, 4 wt% SFG-6 graphite (Timcal), and 2 wt% Super P (Timcal). Subsequent drying and calendaring at 0.5 m min^{-1} resulted in 37% porosity cathodes with $35\text{ }\mu\text{m}$ thick coatings. In addition to fabricated electrodes, virgin $\text{Li}_{1.2}\text{Co}_{0.1}\text{Mn}_{0.55}\text{Ni}_{0.15}\text{O}_2$ material was supplied in powder form for TEM and XRD studies.

Cells for *in situ* XRD studies were built based on 2032 coin cell hardware and modified to allow penetration of the X-rays through the cap of the cell, similar to a previous design [28]. For this purpose, a rather large opening ($\sim 13\text{ mm}$ in diameter) was punched in the coin cell case and then sealed with Kapton® film ($\varnothing 19\text{ mm}$ disk), and vacuum sealing epoxy (Torr Seal®) was applied along the edge of the window to prevent electrolyte leakage. The large area of the Kapton® window allowed for data collection at low 2θ angles of incident beam (Mo $K\alpha$ source). Three thin ($15\text{ }\mu\text{m}$) aluminium strips were placed around Kapton window providing a conductive bridge between the cathode and the stainless steel case of the button cell. The details of the configuration can be found in Ref. [28] with two major differences: the use of larger windows and placement of pre-fabricated electrodes on the Al foil on top of the Kapton window.

Cathodes for half-cell coin cell assembly were punched as 12 mm disks inside an argon filled glove box. Lithium foil (Alfa Aesar, 0.75 mm thick, 99.9%) was used as a counter electrode in the half cell ($\varnothing 12\text{ mm}$ disk). 1.2 M solution of LiPF_6 in EC:EMC (3:7 wt) was used as the electrolyte (Purolyte®). A Celgard 2325 separator (19 mm diameter) was placed between the cathode and anode. The cells were prepared inside a glove box using an automatic crimping machine (Hohsen Corp.). For the *in situ* XRD experiments (setup shown in Fig. 2), a PANalytical X'Pert Pro system was used with Mo $K\alpha$ source ($\lambda = 0.71073\text{ }\text{\AA}$) and automatic divergence and anti-scatter slits. The modified coin cell was placed into the flat 5 mm height PCB holder,

which in turn was affixed into the specially fabricated Lexan fixture with four set screws. The fixture with the cell was attached to a movable stage inside the XRD enclosure. Shielded cables from the potentiostat were fed through a port in the XRD enclosure and attached to the leads of the coin cell holder. This configuration prevents any undesired tilt or displacement of the sample during the scan while allowing data collection at small incident angles. Electrochemical cycling during the *in situ* XRD experiments was performed using a BioLogic SP-200 potentiostat controlled with the EC-Lab software (V. 10.02). The cells were cycled between 2.4 and 4.8 V vs. Li^+/Li at 10 mA g^{-1} (at C/32 rate). In order to investigate the phase transformations occurring in the cathode material after 16 and 36 cycles, the electrodes were cycled in regular half-cell coin cells outside of the XRD chamber and then transferred to the *in situ* coin cells in an argon filled glove box for the *in situ* diffraction experiments.

The collected *in situ* XRD patterns and three *ex situ* XRD patterns (pristine, after 16, and 36 cycles) were refined by the Rietveld method using the X'pert HighScore Plus software with an agreement parameter of $R_p \leq 4\%$, $R_{wp} \leq 7\%$ and goodness of fit (GOF) ≤ 5 . Unit cells of the layered LiMO_2 phase with the $R\bar{3}m$ space group and the Li_2MnO_3 phase with the $C2/m$ space group were refined; detailed crystallographic information of these structures can be found elsewhere [29,30]. The lattice constants were determined by least squares refinements, and the quantitative phase compositions for pristine and after 16(36) cycled samples were calculated using the equation described by Hill and Howard [31].

2.2. *Ex situ* XRD, SEM and TEM

The *ex situ* powder XRD pattern was collected on a PANalytical X'Pert Pro system operated at 60 kV and 45 mA current with Mo $K\alpha$ ($0.71073\text{ }\text{\AA}$) source. The microstructure of the starting electrode was determined using a Hitachi S4800 FEG-SEM operated at 15 kV. Transmission electron microscopy (TEM) for the starting powder was performed using Hitachi HF3300 TEM at 300 kV. For TEM studies, samples were prepared by dispersing as-received starting powder in ethanol and adding a few drops of the suspension to a holey copper grid.

3. Results

3.1. *Ex-situ* structural analysis of parent powder $\text{Li}_{1.2}\text{Co}_{0.1}\text{Mn}_{0.55}\text{Ni}_{0.15}\text{O}_2$

Fig. 3 shows the powder XRD of the as-synthesized lithium-rich NMC material. It is seen that all major peaks in the XRD pattern were indexed by the α - NaFeO_2 structure (ICDD PDF # 00-056-0147) with

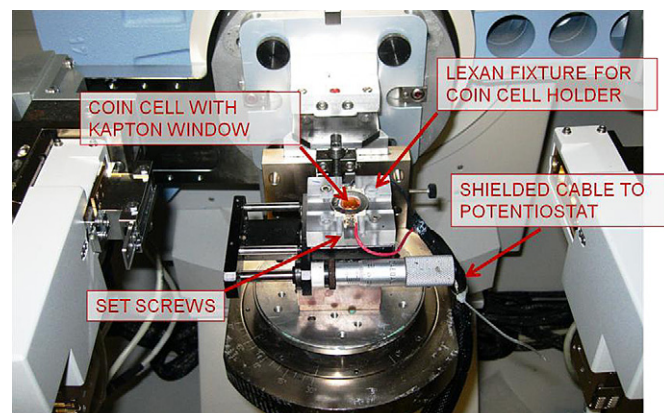


Fig. 2. *In situ* electrochemical XRD set up.

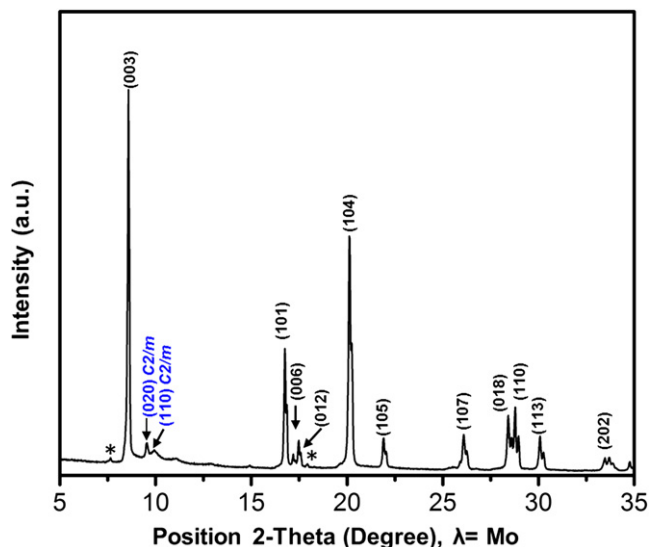


Fig. 3. Powder XRD pattern of $\text{Li}_{1.2}\text{Co}_{0.1}\text{Mn}_{0.55}\text{Ni}_{0.15}\text{O}_2$. The Mo- $\text{K}\beta$ peaks are shown with star marks.

$R\bar{3}m$ space group, except for two weak peaks in the lower 2θ region ($9\text{--}15^\circ$), which are indexed by the $C2/m$ space group (ICDD PDF #04-011-3411). The latter reflections appear due to the ordering of lithium ions with transition metal ions in the transition metal layers and indicate the presence of a second Li_2MnO_3 phase.

The refined c - and a -lattice parameters calculated for the rhombohedral structure were found to be $14.167(3)$ Å and $2.854(3)$ Å with a c/a ratio of 4.99. The clear splitting of (006)/

(012) and (018)/(110) doublets confirm that the material crystallized in the layered structure without formation of any spinel structure [32]. The ratio of $I_{(003)}/I_{(104)}$ was calculated as 1.57 (>1.2), which is also an indication of the formation of a layered structure [32]. Similarly, a lower value of R -factor ($R = [I_{(102)} + I_{(006)}]/I_{(101)}$) in the layered structure is considered as a good estimate for separation of transition metal ions and lithium ions into their respective planes [33]. The R -factor for this material is calculated to be 0.342, which demonstrates the hexagonal ordering (O3 type) in the crystal [34].

In Fig. 4a, a SEM image of the parent lithium-rich NMC material is presented. From the image, it is clear that the particles manifest a platelet-like shape of ~ 1 μm length, in agreement with previously reported morphology of NMC material [35]. Elemental analysis from energy dispersive spectroscopy (EDS) shows the ratio between Co:Mn:Ni to be 0.11:0.54:0.15 in agreement with the targeted composition for this material. A high-resolution TEM micrograph from a representative particle is shown in Fig. 4b. Appearance of distinct lattice fringes confirms good crystallinity of the particles. The distance between two lattice fringes was calculated to be ~ 4.7 Å, which corresponds to (003) planes from the rhombohedral phase and/or (001) planes from the monoclinic phase [11]. Fig. 4c shows single crystal selected area electron diffraction (SAED) collected from the corresponding particle. The experimental SAED pattern consists of three sets of reflections; 1) strong reflections that can be treated as fundamental reflections (marked as solid arrow), 2) weak triplet reflections that appear in between two fundamental reflections (marked as dotted arrow) and 3) much less intense reflections that appear in between the trigonal symmetry axis (marked by a dotted box). The fundamental reflections are from rhombohedral phase and often designated as

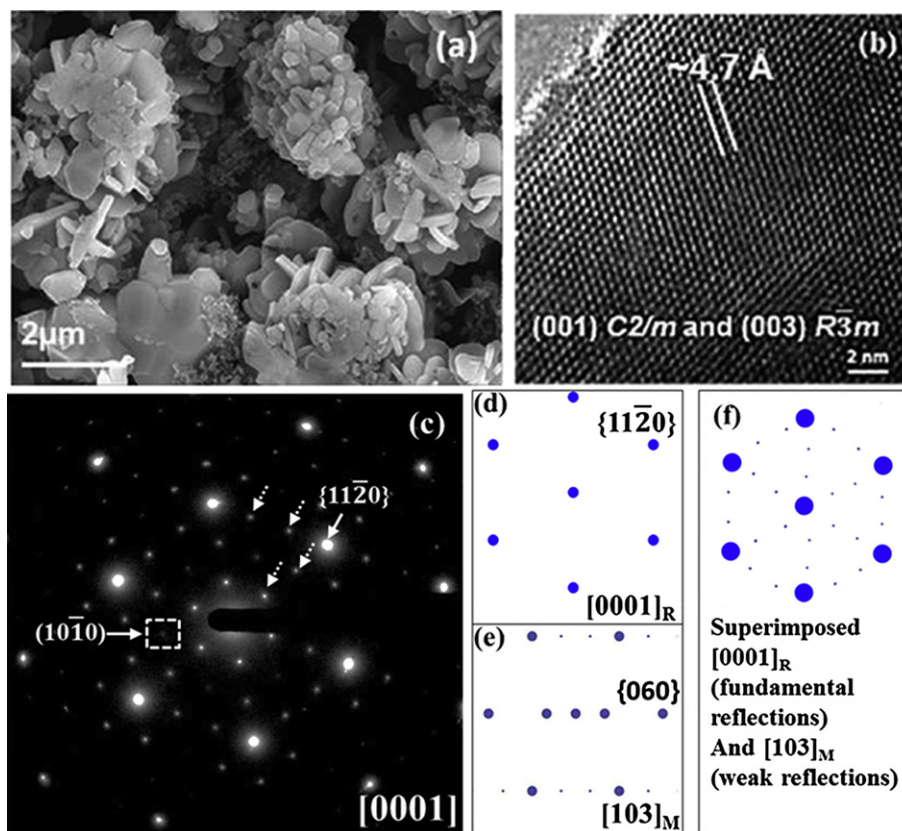


Fig. 4. (a) SEM image, (b) high resolution transmission electron micrograph, (c) experimental SAED pattern along $[0001]$ zone axis of $\text{Li}_{1.2}\text{Co}_{0.1}\text{Mn}_{0.55}\text{Ni}_{0.15}\text{O}_2$, (d) simulated SAED pattern of O3 phase along $[0001]$ zone axis, (e) simulated SAED pattern of monoclinic phase along $[103]$ zone axis, (f) superimposed rhombohedral and monoclinic reflections.

O3 reflections where the lithium ions occupy the octahedra interstitial position with layered ABC...ABC stacking in the unit cell. These reflections appear due to random distribution of the transition metal ions in the transition metal layer 3a sites and lithium in the 3b sites. The appearance of weak triplet reflections suggests the presence of the monoclinic phase and illustrates the ordering of lithium ions with the transition metal ions (Mn ions) in the transition metal layers. These reflections are mainly due to the presence of Li_2MnO_3 -like domains. These two sets of reflections can be thought of as integration of planes from [0001] zone axis of O3 phase (simulated SAED pattern is given in Fig. 4d) and three Li_2MnO_3 monoclinic domains oriented along [103] zone axis (simulated pattern is given in Fig. 4e) rotated 120° about the [0001] zone axis of O3 phase [36]. The simulated pattern of superimposed monoclinic reflections with the O3 reflections is represented in Fig. 4f, in agreement with the experimental SAED pattern.

The third set of reflections is denoted as a forbidden reflection $\{10\bar{1}0\}$ along the [0001] zone axis. The appearance of forbidden reflections suggests that the rhombohedral symmetry is disturbed in some crystals with stacking faults or dislocations. Previous simulation for LiMO_2 ($M = \text{Co}, \text{Mn}, \text{Ni}$) material illustrates that this can be achieved by replacing lithium ions by transition metal ions in the lithium layer [37,38]. These XRD and SAED results confirm the parent $\text{Li}_{1.2}\text{Co}_{0.1}\text{Mn}_{0.55}\text{Ni}_{0.15}\text{O}_2$ material is the integration of both the rhombohedral $\text{LiNi}_{0.375}\text{Co}_{0.25}\text{Mn}_{0.375}\text{O}_2$ and monoclinic Li_2MnO_3 phases as expected. Moreover, Rietveld refinement of the starting material yields 46% of rhombohedral phase (mole percentage) and 54% of monoclinic phase (mole percentage), which is close to the desired 50/50 composition of this material ($0.5\text{LiNi}_{0.375}\text{Co}_{0.25}\text{Mn}_{0.375}\text{O}_2 - 0.5\text{Li}_2\text{MnO}_3$).

3.2. In situ XRD analysis of the electrode during the first cycles

In situ XRD experiments were performed during electrochemical lithiation/delithiation within the voltage range of 2.4–4.8 V with a rate of 10 mA g^{-1} . For analytical purposes, the voltage range was divided into five regions. Region I_C represents charging from open circuit voltage (or 2.4–4.4 V); region II_C spans the plateau region from 4.4 to 4.6 V; region III_C covers the end of charge in the high voltage range from 4.6 to 4.8 V; region I_D represents high voltage discharging from 4.8 to 3.5 V, and region II_D covers the low voltage discharge from 3.5 to 2.4 V. The subscripts “C” and “D” represent the charging and discharging processes, respectively. These abbreviations will be used for all results in this report when required.

An *in situ* XRD cell containing the fresh lithium-rich NMC cathode with lithium foil showed an initial open-circuit voltage (OCV) of about 2.7 V. Fig. 5 shows the *in situ* XRD patterns of the cathode material undergoing the first 1.5 cycles. Different colour stacks represent the corresponding electrochemical delithiation and lithiation processes as shown on right side of the figure. In Fig. 5, all the peaks in the XRD pattern show the characteristic reflections of the rhombohedral phase and were indexed similar to the *ex situ* XRD pattern. The intensities of (101) and (104) Bragg reflections decrease during charging, and the process was found to be reversible during discharging. The (101) and (104) planes contain lithium ions and the decrease/increase in intensities during charging/discharging confirms the successful extraction/insertion of lithium ions from/into the structure (For interpretation of the references to color in this paragraph, the reader is referred to the web version of this article.).

For detailed observations of the peak positions during electrochemical cycling, time resolved isoplots of the (003), (101), (012), (104), and (113) Bragg reflections are presented along with the

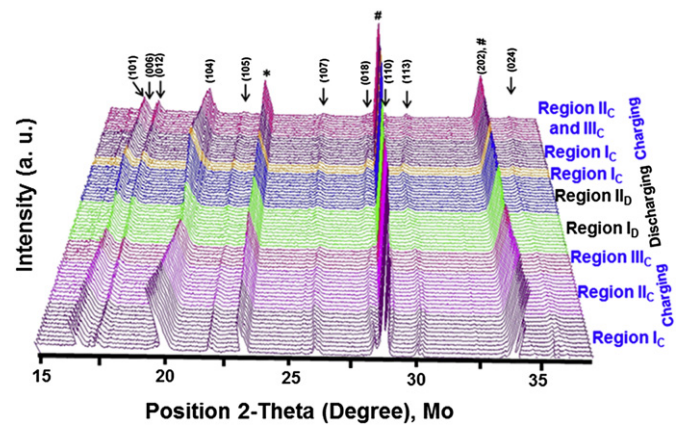


Fig. 5. *In situ* XRD pattern collected from as assembled electrode. The corresponding region of charge/discharge voltage (refer text for details) for 1.5 cycles is shown in right. The reflection from stainless steel (cell cap) and Al from the current collector are designated as * and # respectively.

electrochemical voltage profile in Fig. 6a. The electrochemical data in this study are represented as voltage versus time in order to correlate with the time-resolved XRD patterns. Detailed observations are presented in the following subsections.

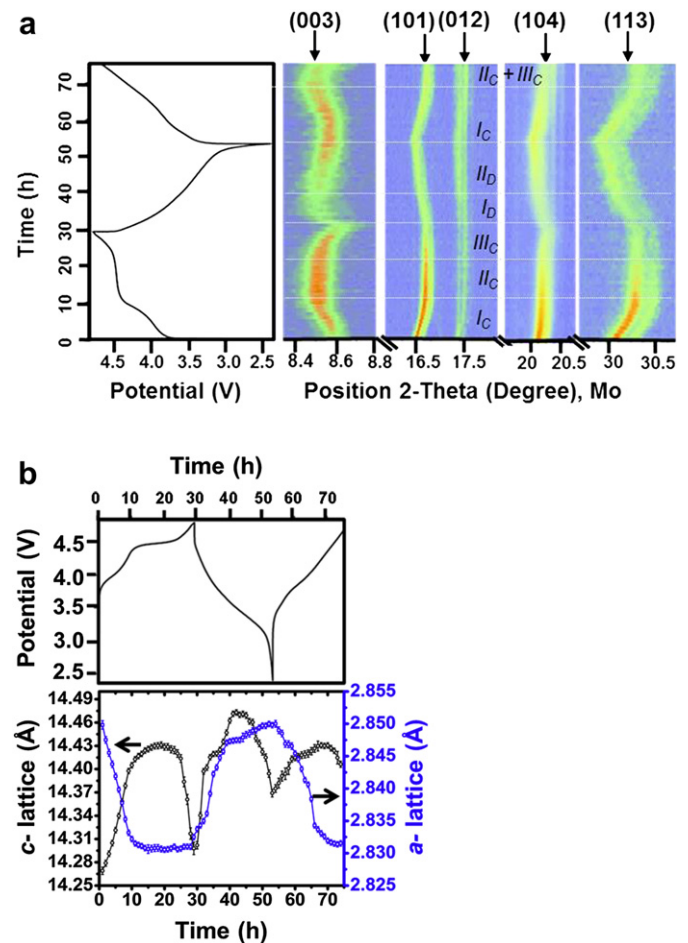


Fig. 6. a) Intensity plots of (003), (101), (012), (104), and (113) peaks along with the electrochemical profile of the cell during the first 1.5 cycles. (b) Change in lattice parameters (with error bars) as a function of electrochemical charge/discharge profile. These plots were collected over the first 1.5 cycles on a cell containing $\text{Li}_{1.2}\text{Co}_{0.1}\text{Mn}_{0.55}\text{Ni}_{0.15}\text{O}_2$ cathode material.

During charging: 1) The (003) peak shifts to lower 2- θ angle in the region I_C, but this displacement is not prominent in the region II_C. The (003) peak shifts to higher 2- θ angle on further charging in the region III_C. 2) The difference in lattice spacing between (101) and (012) planes decreases in the region I_C–III_C, and the (101) peak shifts towards lower 2- θ angle. 3) The (104) and (113) peaks move to higher 2- θ angle in the region I_C–III_C.

During discharging: 1) (003) peak shifts towards the lower 2- θ angle in the region I_D and to higher 2- θ angle in the region II_D (down to 2.4 V). 2) The difference in lattice spacing between (101) and (012) decreases. 3) The (104) and (113) reflections shift to lower 2- θ angle.

In Fig. 6b the lattice parameters calculated from Rietveld analysis are shown along with the electrochemical data. The *c*- and *a*-lattice parameters for lithium-rich NMC at the beginning of the *in situ* experiment were calculated to be 14.27 Å and 2.85 Å respectively. It should be noted that the value of the *c*-lattice parameter of the material in the coin cell was higher than that calculated from *ex situ* powder XRD. A similar phenomenon was observed previously [39] and referred to minor structural changes, possibly electrochemical in nature induced during cell assembly which might be the case here. In the region I_C, the *c*-parameter increases as evidenced by the displacement of the (003) peak (Fig. 6). In this voltage region, lithium ions are extracted from the lithium layers since the energy required to remove the lithium ions from the lithium layers is less than the energy required to remove them from the transition metal layers [12]. The extraction of lithium ions from the lithium layer eventually increases the electrostatic repulsion between the oxygen layers, which causes unit cell expansion along the *c*-axis, hence shifting the (003) peak position to higher *d*-spacing values. Within this region (region I_C), the *a*-parameter decreases. This is attributed to the decrease in average metal–metal distance due to formation of ions having smaller effective ionic radii. In Li_{1.2}Co_{0.1}Mn_{0.55}Ni_{0.15}O₂, Ni²⁺ and Co³⁺ are the electrochemically active ions in this voltage window [14] and the charge compensation during lithium extraction was accompanied by the oxidation of Ni²⁺ (0.69 Å) and Co³⁺ (0.61 Å) to Ni³⁺ (0.56 Å)/Ni⁴⁺ (0.48 Å) and Co⁴⁺ (0.53 Å) respectively in MO₆ environment. In the region II_C (plateau region), the *c*-lattice parameter increases smoothly, and the *a*-parameter remains constant, which suggests that within the plateau region, the average ionic radii of the transition metal ions remain the same. Hence, the charge compensation must occur by another source, possibly during oxygen release (see Discussion Section 4 below). In the region III_C, the *c*-parameter decreases, indicating that the lithium ions are being extracted between the lithium layers (from the transition metal layers).

During discharge, in region I_D, the *c*-parameter increases, which is in agreement with the shifting of the (003) peak position towards lower 2- θ values. This is an indication of expansion of the unit cell along the *c*-axis during lithium insertion into the transition metal layers in the voltage range of 4.8–3.5 V. Similar observations were made regarding lithium-rich oxide cathodes by Lu et al. [23]. The increase in the *a*-axis in this voltage window is due to reduction of Ni²⁺/Ni⁴⁺ and Co⁴⁺ to Ni²⁺ and Co³⁺ respectively. During low voltage lithiation (region II_D), the *c*-axis decreases, which is in accordance with the change in position of the (003) reflection. This indicates the filling of vacancies in the lithium layer by lithium ions, which decrease the electrostatic repulsion among oxygen layers and hence, contraction of unit cell along *c*-axis occurs. The shifting of the (104), (113), and (104) peak positions is similar to the observations of previous studies on lithium-rich oxide compounds [24].

3.3. *In situ* XRD analysis after subsequent electrochemical cycles

Two cells were cycled for 16 and 36 times respectively, and the cathodes were transferred to *in situ* XRD cells to perform the *in situ*

experiments. The *ex situ* cycling was done at the same rate and within the same voltage range as in the case of *in situ* experiments. The *c*- and *a*-lattice parameters for lithium-rich NMC were determined to be 14.48 ± 0.02 Å and 2.855 ± 0.001 Å respectively with an OCV of 3.5 V (after 16 cycles) and 14.48 ± 0.02 Å and 2.850 ± 0.001 Å with an OCV of 3.6 V (after 36 cycles). These values are higher than the lattice parameter values for fresh electrode measured before electrochemical charge/discharge cycling (see Section 3.2). This finding reveals the irreversible expansion of the unit cell of the present lithium-rich NMC during subsequent cycles. The expansion of the unit cell during repeated charge/discharge cycles may be due to (1) strain and/or lithium deficiency in the cathode material during the delithiation/lithiation process and/or (2) an electrostatic repulsion across the van der Waals gap between the transition metal oxide sheets [40]. This *c*-lattice parameter did not increase significantly after 36 cycles as compared to the cell cycled 16 times, which confirms that lattice distortion occurs mainly during the initial electrochemical cycles [35]. A slight decrease in the *a*-parameter after 16 and 36 cycles may be due to a minor change in the average oxidation states of transition metal ions, consistent with previously reported data for lithium-rich oxide systems [40]. The positions of the (003), (101), (102), (104) and (103) Bragg peaks with the corresponding electrochemical cycling voltage profile after 16 and 36 cycles are presented in Figs. 7a and 8a, respectively. The measured lattice parameters are presented in Fig. 7b (after 16 cycles) and Fig. 8b (after 36 cycles). The (101), (102), (104), and (113) peaks show similar behaviour during charging/discharging as compared to freshly assembled electrodes. The (003) peak shifts to lower 2- θ values corresponding to an increase in *c*-parameter values in the region I_C. The *a*-lattice also contracts within this region revealing the oxidation of metal ions as explained above. These results are similar to results obtained from the first cycle. However, beyond this region the (003) peak shifts rapidly towards the higher 2- θ values, in contrast to the fresh electrode where a smooth shift was observed. This transition is also reflected in the *c*-lattice values; beyond region I_C a rapid decrease in *c*-parameter was observed as opposed to the gradual decrease observed during the first 1.5 cycles of a freshly assembled cell. During further charging beyond the region I_C, the *a*-lattice value increases, unlike the fresh electrode where a constant *a*-lattice value was observed in the region II_C. It is also noted that during the second charging process in the voltage range 2.4–3.5 V, the *c*-lattice values decrease, which is also in accordance with the position of the (003) peaks (see the highlighted area in Figs. 8a and 9a). The reason for this behaviour is unclear. However, it is believed that after subsequent cycles, the present Li-rich material requires longer time to equilibrate during low voltage discharging and/or spinel phase formation during low discharge/charge process (see below).

During discharge, the observation of (003), (101), (012), (104), and (113) was very much similar to the results obtained from fresh cell. However, interestingly, new peaks at ~28.32° 2- θ appear after 16 and 36 cycles (Fig. 9b and c, highlighted in dotted circle) during low voltage discharge (3.5–2.4 V; region II_D), which are absent in the first 1.5 cycles (Fig. 9a). These peaks remain during low voltage charging (2.4–3.5 V) and then disappear when charging beyond that voltage. These reflections are characteristic (440) peak of AB₂O₄ spinel phase (ICDD PDF # 00-018-0736) possibly due to the presence of LiMn₂O₄. For better representation, selected XRD patterns with normalized intensity in 3.5–2.4 V discharge voltage region are shown in Fig. 10, where the appearance of spinel peaks is clearly observed after 16 and 36 cycles. Since the major reflections from LiMn₂O₄ spinel merge with the reflections from trigonal phase, the (004) peak was taken as the reflection to differentiate the spinel phase from the layered phase.

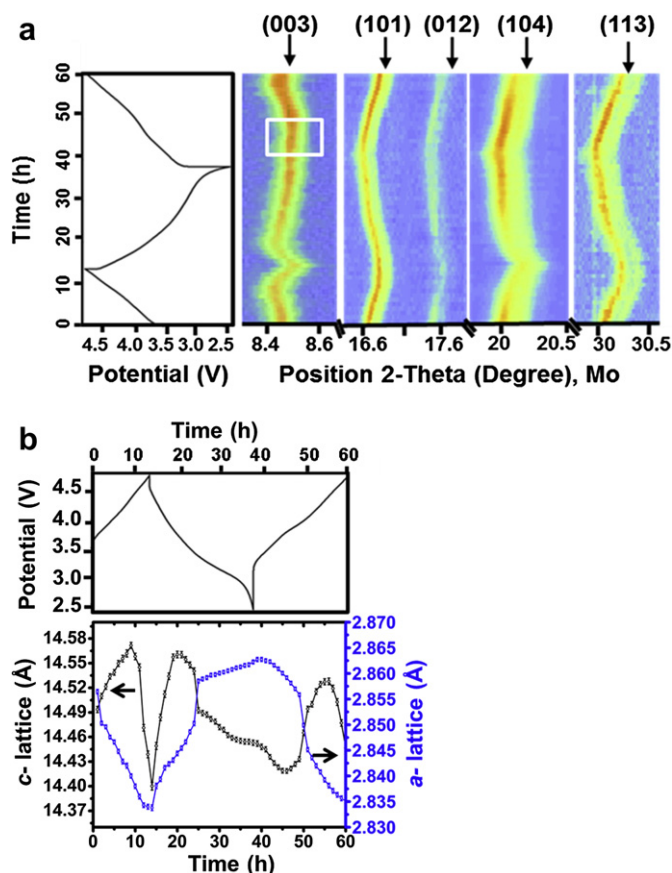


Fig. 7. (a) Isoplots of (003), (101), (012), (104), and (113) peak positions along with the electrochemical profile. These plots were collected from the cell after 16 cycles containing $\text{Li}_{1.2}\text{Co}_{0.1}\text{Mn}_{0.55}\text{Ni}_{0.15}\text{O}_2$ as cathode material. (b) Change in lattice parameter (with error bars) as a function of electrochemical charge/discharge profile. These plots were collected from the cell after 16 cycles containing $\text{Li}_{1.2}\text{Co}_{0.1}\text{Mn}_{0.55}\text{Ni}_{0.15}\text{O}_2$ as cathode material.

The overall structure still remains layered, hence it is expected that smaller size spinel domains may have been created in the crystals and locally integrated into the layered framework. The monoclinic (13 $\bar{3}$) peak also disappeared after subsequent cycling (Fig. 9). Quantitative Rietveld analysis was conducted on higher-quality *ex-situ* XRD data collected on one pristine and two cycled (16 and 36 cycles) electrodes as explained in the Experimental section. The observed monoclinic phase was 64% trigonal and 36% monoclinic after 16 cycles and 72% trigonal and 28% monoclinic after 36 cycles, as compared to 46% trigonal and 54% monoclinic phase for the fresh electrode. The fraction of spinel phase was so small that it could not be adequately refined in the Rietveld analysis. However, it is believed that the spinel phase was formed at the expense of the monoclinic phase. The presence of spinel phase may alter the voltage profile in 16(36) cycles which is discussed below in the Discussion section.

4. Discussion

Fig. 11 shows the voltage profiles (electrode potential vs. capacity) of the material under investigation collected during the 1st, 16th, and 36th cycles in the voltage window of 2.4–4.8 V. The cell shows a first cycle charge capacity of 303 mA h g^{-1} and discharge capacity of 232 mA h g^{-1} at 10 mA h g^{-1} rate. A first cycle irreversible capacity of $\sim 70 \text{ mA h g}^{-1}$ with a first cycle efficiency of $\sim 77\%$ was observed. The structural changes during lithium

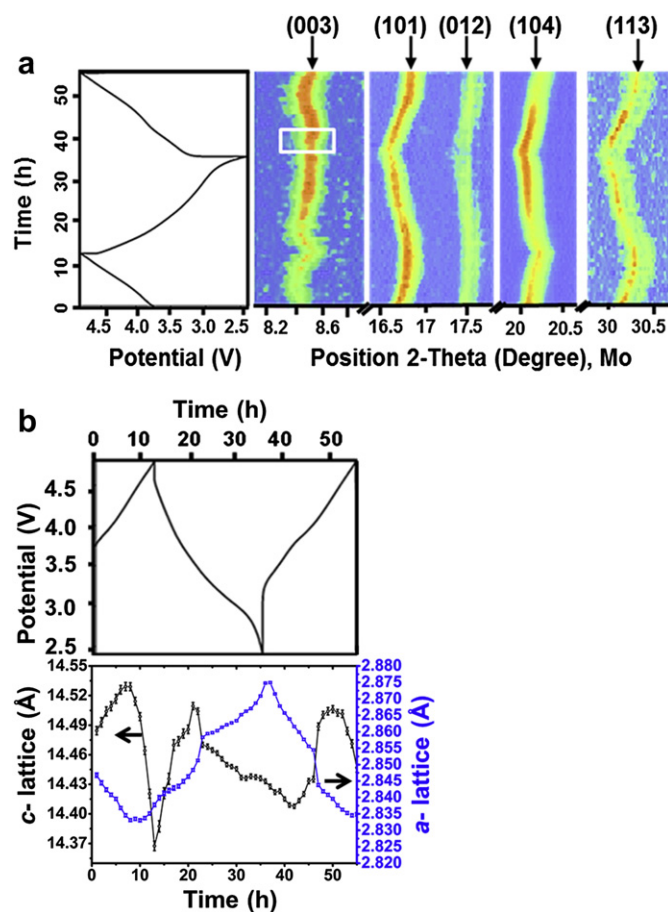


Fig. 8. (a) Isoplots of (003), (101), (012), (104), and (113) peak positions along with the electrochemical profile. These plots were collected from the cell after 36 cycles containing $\text{Li}_{1.2}\text{Co}_{0.1}\text{Mn}_{0.55}\text{Ni}_{0.15}\text{O}_2$ as cathode material. (b) Change in lattice parameter (with error bars) as a function of electrochemical charge/discharge profile. These plots were collected from the cell after 36 cycles containing $\text{Li}_{1.2}\text{Co}_{0.1}\text{Mn}_{0.55}\text{Ni}_{0.15}\text{O}_2$ as cathode material.

extraction and insertion are schematically represented in Fig. 12. During initial charging, lithium ions are continuously extracted from the lithium layer, contributing to an increase in capacity up to the cell voltage of 4.4 V (Fig. 12b). Up to this voltage range, the trigonal phase is electrochemically active and lithium ion extraction from the trigonal phase increases the electrostatic repulsion among the cubic closed packed oxygen layers; as a result of this, the *c*-axis expands (Fig. 6). In this region, the charge compensation reaction is explained by oxidation of Co^{3+} to Co^{4+} and Ni^{2+} to $\text{Ni}^{3+}/\text{Ni}^{4+}$, which decreases the average metal–metal distances and, eventually, the *a*-axis contracts. Beyond 4.4 V, a pronounced voltage plateau is observed in the voltage window of 4.4–4.6 V, where the charge capacity increases up to $\sim 260 \text{ mA h g}^{-1}$. It is expected that at this voltage, the Li_2MnO_3 phase is activated, and removal of lithium from the transition metal layer occurs, which is accompanied by the simultaneous removal of oxygen from the structure (Fig. 12c). This reaction can be represented as $\text{Li}_2\text{MnO}_3 \rightarrow \text{Li}_2\text{O} + \text{MnO}_2$. The removal of lithium from the transition metal layer (Li_2O) is in agreement with the *c*-axis contraction observed after charging beyond 4.4 V. It was also observed that the *a*-lattice parameter remains constant above 4.4 V, which indicates that the average oxidation states of transition metal ions do not change in the 4.4–4.6 V region. If the oxidation states of the transition metal ions do not change, the charge compensation must be accompanied by the release of oxygen from the structure, which is

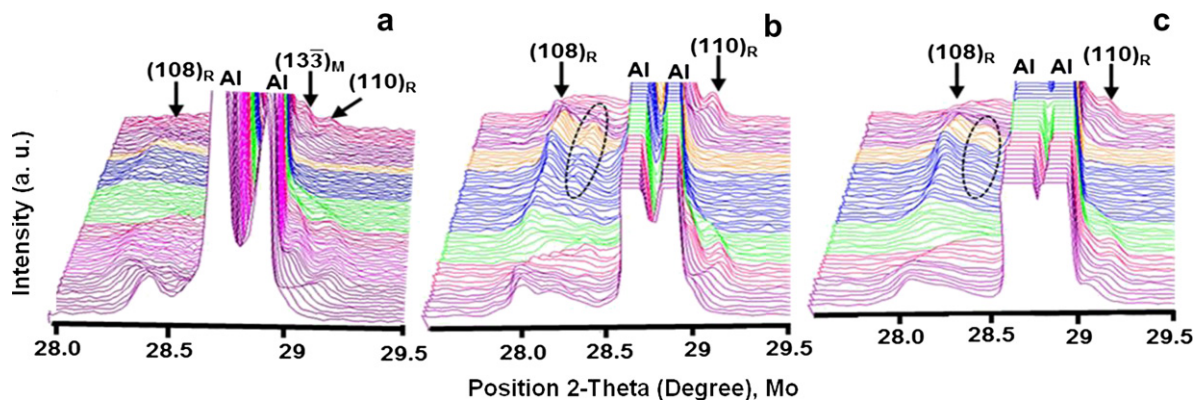


Fig. 9. (108), (110), (133) reflection during first 1.5 cycles (a), after 16 cycles (b) and after 36 cycles (c). The R and M subscripts designate the rhombohedral (trigonal) phase and monoclinic phase respectively. The colour stacks are similar to Fig. 5. The appearance of new peaks is highlighted in the dotted regions.

believed to occur due to activation of the Li_2MnO_3 phase (beyond 4.4 V). It can be hypothesized, that the extraction of Li_2O likely contributes towards the irreversible capacity that was observed in the 1st cycle. This result is similar to studies reported for other lithium-rich oxides [12,21,41]. It is also anticipated that at high voltage (beyond 4.4 V), migration of transition metals from the transition metal layer to the lithium layer may take place [19]. This may reduce the electrostatic repulsion among oxygen layers to shrink the *c*-parameter (Fig. 12d). During the discharge process to 3.5 V, the *c*-lattice increases, which indicates the filling of vacancies in the transition metal layer (Fig. 12e). Discharging below 3.5 V causes the *c*-lattice value to decrease, which accompanies a decrease in electrostatic repulsion among oxygen layers due to filling of vacancies in the lithium layer (Fig. 12f). The *a*-lattice values increase during discharge, which confirms an increase in average metal–metal distance due to formation of Ni^{2+} and Co^{3+} ions from Ni^{4+} and Co^{4+} respectively.

It was observed that the discharge capacity decreased to 223 mA h g^{-1} and 206 mA h g^{-1} after subsequent 16 and 36 cycles, respectively. After 36 cycles, ~10% further loss in discharge capacity was observed as compared to the first cycle discharge capacity. However, the discharge voltage plateau shifted towards the lower voltage profile (represented as arrow mark in Fig. 11). This phenomenon is often termed as “voltage decay/fade”. As explained above, this voltage decay might be directly related to the formation of spinel phase (domains) that was observed after 16(36) cycles. The structural evolution from layered to spinel in the layered oxygen network in this lithium-rich oxide material may alter the lithium deintercalation/intercalation process. Therefore, after 16 or

36 cycles, the lithium extraction/insertion could occur at a different potential (voltage) as compared to the first cycle where only the layered structure is present which could be the reason for voltage decay after subsequent cycling. In fact, the transformation of layered to spinel phase after subsequent cycles is not aberrant in lithium containing layered oxide with an excess manganese composition, as reported by others [22,43]. However, the structural transformation observed in $\text{Li}_{1.2}\text{Co}_{0.1}\text{Mn}_{0.55}\text{Ni}_{0.15}\text{O}_2$ after subsequent cycles in the present study provides the reason for discharge voltage fading in this highly efficient cathode. This formation of the spinel phase has to be controlled by modifying the parent structure in order to overcome the voltage fading barrier, but the associated formation mechanism is not yet fully understood. However, it is anticipated that migration of transition metal cations/lithium ion from their crystallographic sites to other available sites in the unit cell during charge/discharge process might change the cation ordering in the structure and possibly form the spinel phase in some regions. The site occupancy factor (SOF) refinement of Li/TM on *in situ* XRD patterns resulted in no significant difference in the overall refinement, because of less sensitivity of X-rays towards lower mass elements. We are currently pursuing neutron diffraction, TEM, and magnetic susceptibility experiments to obtain the detail crystallographic information on these phase transformed products of Li-rich cathodes and the results will be presented in future publications.

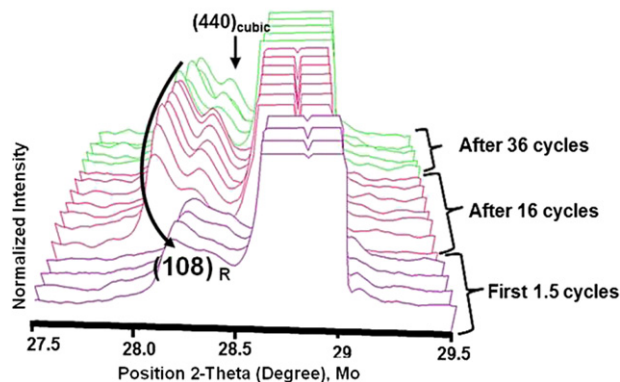


Fig. 10. Normalized intensity XRD patterns of $\text{Li}_{1.2}\text{Co}_{0.1}\text{Mn}_{0.55}\text{Ni}_{0.15}\text{O}_2$ cathode during first 1.5 cycles, after 16 cycles and after 36 cycles. The patterns were selected in the region of 3.5–2.4 V discharge. After 16(36) cycles, the spinel peak appeared.

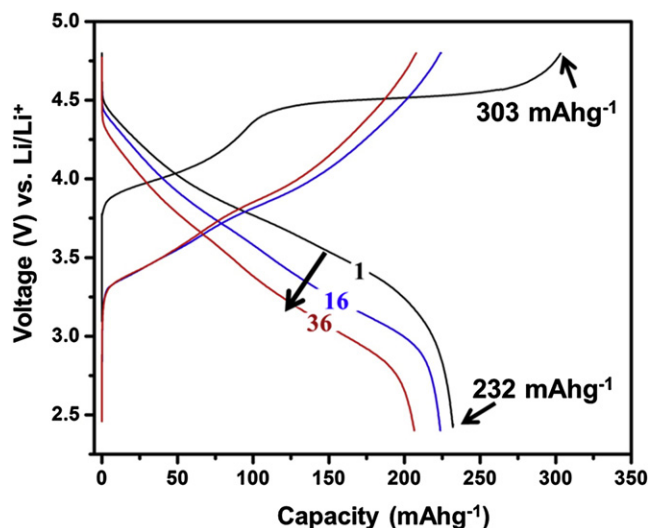


Fig. 11. Galvanostatic charge/discharge profiles of lithium rich NMC cathode.

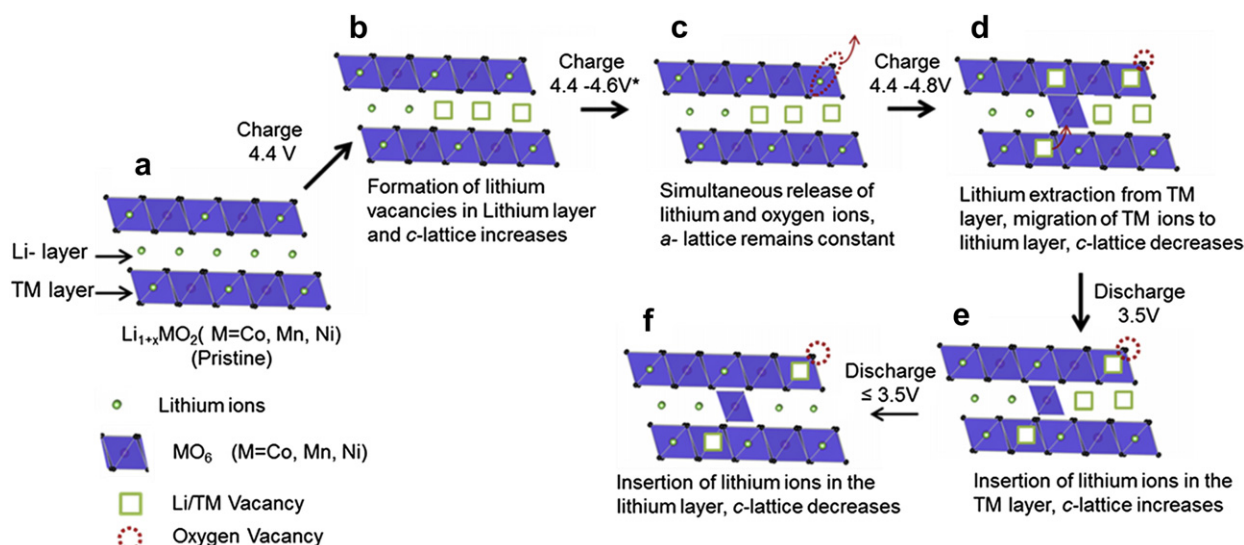


Fig. 12. Schematic of change in crystal structure of $\text{Li}_{1.2}\text{Co}_{0.1}\text{Mn}_{0.55}\text{Ni}_{0.15}\text{O}_2$ in the course of charge/discharge process (see text for explanation). The model was drawn by using VESTA [42]. *Only observed for the first cycle.

5. Conclusions

The structural transformation of $\text{Li}_{1.2}\text{Co}_{0.1}\text{Mn}_{0.55}\text{Ni}_{0.15}\text{O}_2$ (Toda HE5050) cathode during high voltage cycling was observed by *in situ* XRD. The change in lattice parameters during electrochemical delithiation/lithiation was monitored for the first cycle and up to 36 cycles. During the course of charging at high voltage (above 4.4 V), the *c*-lattice parameter decreases for the first cycle and after subsequent cycles, which demonstrates the activation of the Li_2MnO_3 phase with migration of transition metal ions from transition metal layers to lithium layers. At the plateau region in the first cycle, the *a*-lattice parameter remained constant, which was not observed in the cells after subsequent cycling. This finding is attributed to simultaneous release of oxygen and lithium ions during the first cycle, which contributes to the high irreversible capacity loss. During discharge process, the *c*-lattice parameter increases initially up to 3.5 V and then decreases further discharging below 3.5 V indicating the insertion of lithium ions in the latter case. After subsequent cycles, a (440) cubic spinel reflection appears during discharge process which was not previously observed. This finding reveals the layered to the spinel-like phase transformation and is believed to be the reason for the depression in the discharge voltage plateau during electrochemical cycling. In order to overcome this voltage fading barrier, the formation of the spinel phase must be controlled by modifying the composition/structure of parent material and/or by doping with different stabilizing cations. The related significant decrease of the monoclinic phase observed after subsequent cycles may contribute to structural instability after repeated cycling.

Acknowledgement

The electrodes in this study were produced at the U.S. Department of Energy's (DOE) Cell Fabrication Facility, Argonne National Laboratory (ANL). The Cell Fabrication Facility is fully supported by the DOE Vehicle Technologies Program (VTP) within the core funding of the Applied Battery Research (ABR) for Transportation Program. This research at Oak Ridge National Laboratory, managed by UT Battelle, LLC, for the U.S. Department of Energy under contract DE-AC05-00OR22725, was sponsored by the Vehicle Technologies Applied Battery Research Program (Program

Manager: Peter Faguy) of the Office of Energy Efficiency and Renewable Energy. The TEM work was performed at Oak Ridge National Laboratory thru ShaRE user facility. Authors thank to Dr. Daniel Abraham at ANL for useful discussion.

References

- [1] C. Daniel, JOM 60 (2008) 43.
- [2] J.-M. Tarascon, M. Armand, Nature 414 (2001) 359.
- [3] D. Mohanty, P. Paudel, H. Gabrisch, Solid State Ionics 181 (2010) 914.
- [4] D. Zeng, J. Cabana, W.-S. Yoon, C.P. Grey, Chemistry of Materials 22 (2010) 1209.
- [5] K. Mizushima, P.C. Jones, P.J. Wiseman, J.B. Goodenough, Materials Research Bulletin 15 (1980) 783.
- [6] D. Mohanty, H. Gabrisch, Solid State Ionics 194 (2011) 41.
- [7] A.J. Manthiram, Journal of Physical Chemistry Letters 2 (2011) 176.
- [8] K.-W. Nam, W.-S. Yoon, H. Shin, K.Y. Chung, Journal of Power Sources 191 (2009) 652.
- [9] J. Breger, Y.S. Meng, Y. Hinuma, S. Kumar, K. Kang, Chemistry of Materials 18 (2006) 4768.
- [10] C.S. Johnson, N. Li, C. Lefief, M.M. Thackeray, Electrochemistry Communications 9 (2007) 787.
- [11] M.M. Thackeray, C.S. Johnson, J.T. Vaughey, N. Li, S.A. Hackney, Journal of Materials Chemistry 15 (2006) 2257.
- [12] C.S. Johnson, N. Li, C. Lefief, J.T. Vaughey, M.M. Thackeray, Chemistry of Materials 20 (2008) 6095.
- [13] C.S. Johnson, J.S. Kim, C. Lefief, N. Li, J.T. Vaughey, M.M. Thackeray, Electrochemistry Communications 6 (2004) 1085.
- [14] S.K. Martha, J. Nanda, G.M. Veith, N.J. Dudney, Journal of Power Sources 199 (2012) 220.
- [15] N. Yabuuchi, K. Yoshii, S.-T. Myung, I. Nakai, S. Komaba, Journal of American Chemical Society 133 (2011) 4404.
- [16] S.J. Jin, K.S. Park, M.H. Cho, C.H. Song, A.M. Stephan, K.S. Nahm, Solid State Ionics 177 (2006) 105.
- [17] F. Amalraj, D. Kovacheva, M. Talianker, L. Zeiri, J. Grinblat, N. Leifer, G. Goobes, B. Markovsky, D. Aurbach, Journal of The Electrochemical Society 157 (2010) A1121.
- [18] K.A. Jarvis, Z. Deng, L.F. Allard, A. Manthiram, P.J. Ferreira, Chemistry of Materials 23 (2011) 3614.
- [19] B. Xu, C.R. Fell, M. Chi, Y.S. Meng, Energy and Environmental Science 4 (2011) 2223.
- [20] S.-H. Kang, P. Kempgens, S. Greebaum, A.J. Kropf, K. Amine, M.M. Thackeray, Journal of Materials Chemistry 17 (2007) 3112.
- [21] Q.Y. Wang, J. Liu, A.V. Murugan, A. Manthiram, Journal of Materials Chemistry 19 (2009) 4965.
- [22] A.R. Armstrong, N. Dupre, A.J. Paterson, C.P. Grey, P.G. Bruce, Chemistry of Materials 16 (2004) 3106.
- [23] Z. Lu, J.R. Dahn, Journal of The Electrochemical Society 149 (2002) A815.
- [24] C.R. Fell, M. Chi, Y.S. Meng, J.L. Jones, Solid State Ionics 207 (2012) 44.
- [25] M. Balasubramanian, X. Sun, X.Q. Yang, J. McBreen, Journal of Power Sources 92 (2001) 1.

- [26] M.N. Richard, I. Koetschau, J.R. Dahn, *Journal of The Electrochemical Society* 144 (1997) 554.
- [27] K. Rhodes, M. Kirkham, R. Meisner, C.M. Parish, N. Dudney, C. Daniel, *Review of Scientific Instruments* 82 (2011) 075107.
- [28] K. Rhodes, R. Meisner, Y. Kim, N. Dudney, C. Daniel, *Journal of The Electrochemical Society* 158 (2011) A890.
- [29] J. Akimoto, Y. Gotoh, Y. Oosawa, *Journal of Solid State Chemistry* 141 (1998) 298.
- [30] P. Strobel, B.L. Andron, *Journal of Solid State Chemistry* 75 (1998) 90.
- [31] R.J. Hill, C.J. Howard, *Journal of Applied Crystallography* 20 (1987) 467.
- [32] Z.H. Lu, L.Y. Beaulieu, R.A. Donaberger, C.L. Thomas, J.R. Dahn, *Journal of The Electrochemical Society* 149 (2002) A778.
- [33] J.R. Dahn, U. Sacken, C.A. Michal, *Solid State Ionics* 44 (1990) 87.
- [34] X. Luo, X. Wang, L. Liao, X. Wang, S. Gamboa, P.J. Sebastian, *Journal of Power Sources* 161 (2006) 601.
- [35] J. Hong, D.-H. Seo, S.-W. Kim, H. Gwon, S.-T. Ohb, K. Kang, *Journal of Materials Chemistry* 20 (2010) 10179.
- [36] J. Barevo, M. Balasubramanian, S.H. Kang, J.G. Wen, C.H. Lei, S.V. Pol, I. Petrov, D.P. . Abraham, *Chemistry of Materials* 23 (2011) 2039.
- [37] H. Gabrisch, T. Yi, R. Yazami, *Electrochemical and Solid-State Letters* 11 (2008) A119.
- [38] D. Mohanty, H. Gabrisch, *Journal of Power Sources* 220 (2012) 405.
- [39] N. Sharma, M.V. Reddy, G. Du, S. Adams, B.V.R. Chowdari, Z. Guo, V.K. Paterson, *Journal of Physical Chemistry* 15 (2011) 21473.
- [40] J. Choi, A. Manthiram, *Journal of The Electrochemical Society* 152 (2005) A1714.
- [41] D. Kim, J. Gim, J. Lim, S. Park, J. Kim, *Materials Research Bulletin* 45 (2010) 252.
- [42] K. Momma, F. Izumi, *Journal of Applied Crystallography* 41 (2008) 653.
- [43] A.R. Armstrong, P.G. Bruce, *Nature* 381 (1996) 499.